Wideband Dissipativity Enhancement of Grid-Following Inverters Using Virtual Element Design

Yang, Zhiqing; Wu, Wei; Li, Helong; Ding, Lijian; He, Shan; Blaabjerg, Frede

Published in:
CPSS Transactions on Power Electronics and Applications (CPSS TPEA)

DOI (link to publication from Publisher):
10.24295/CPSSTPEA.2023.00026

Publication date:
2023

Document Version
Publisher's PDF, also known as Version of record

Wideband Dissipativity Enhancement of Grid-Following Inverters Using Virtual Element Design

Zhiqing YANG, Wei WU, Helong LI, Lijian DING, Shan HE, and Frede BLAABJERG

***Abstract*—Dissipativity provides a convenient approach to predict system stability, which explains the induced resonances from the perspective of damping. To mitigate potential resonances and improve stability, this work presents a design method to enhance the dissipativity of grid-following inverters over a wide frequency range. Based on the *dq*-domain admittances, the frequency-domain dissipativity affected by different control loops and the time delay are investigated. By designing virtual elements, the dissipativity in different frequencies can be flexibly enhanced. A model-based design criterion is proposed to tune the control parameters following a model-based approach. The design method is presented for a high-power inverter system. The effectiveness of the method is also proved with a down-scaled prototype, which includes simulations, experiments, and dissipativity analysis.**

***Index Terms*—Control design, dissipativity, grid-following inverter, resonances, stability, virtual admittance.**

I. Introduction

WIDEBAND resonances occur in grid-following inverter systems due to dynamic interactions among the inverters and the grid [1], [2]. The poorly damped resonances may sustain itself at a constant magnitude, or even grow boundlessly, leading to a shutdown of systems, which may significantly threaten the grid security [3].

To identify the cause of resonances and evaluate system stability, different approaches are available. From the perspective of control theory, a system can be analyzed with conventional stability criteria, such as Bode criterion [4], [5] or Nyquist criterion [4], [6]. To further simplify the calculations, criteria based on impedance specifications are developed, such as forbidden-region criterion [7], [8], which avoids the calculation of eigenvalues. In addition to that, the stability can also be investigated with a net-damping criterion based on the passivity theory [9], [10]. The passivity theory provides an intuitive approach in the frequency domain to analyze potential resonances from the perspective of dissipation [11].

The dissipativity plays an important role to guarantee stability, as resonances dissipate if the system is passive, i.e., can provide sufficient damping, at potential resonant frequencies [11]. However, non-dissipative region is observed over a wide frequency range in grid-following inverter systems, which can induce wideband resonances or even jeopardize system stability. Due to the phase-locked loop (PLL), non-dissipative area occurs within its bandwidth for the inverter-mode operation, which has a negative impact especially under a weak grid [4], [11]. The direct-voltage control (DVC) induces non-dissipative region below its bandwidth either for the rectifier-mode operation [4], [11], or for high-power operations in the inverter mode [6]. Dissipativity may deteriorate due to the interaction of the PLL and DVC, if their bandwidths are not properly designed [12]. In addition, the delay time induced by digital control can result in high-frequency non-dissipative area [13]–[18]. To eliminate resonances and improve stability, different control schemes are developed to improve system dissipation, which can be categorized into two aspects.

The first aspect focuses on the non-dissipative area introduced by the time delay, which is usually beyond the inner-loop bandwidth [13]–[18]. An active damping scheme with the derivative voltage feedforward is proposed to enhance the high-frequency dissipativity, where the derivative gain is determined by the delay time [13], [14]. A virtual-flux-based approach is proposed to improve dissipation with an integral voltage feedforward [15]. The damping gain is designed according to the control and filter parameters. Besides, an active damping scheme is studied in [16] based on the proportional current feedback with a bi-quad filter. The delay-induced non-dissipative region can also cause resonances in grid-forming inverters [17]. Resistive components are preferred in some cases to extend the dissipative region, though the system losses increase simultaneously [14], [18]. However, as models are simplified, there is no discussion in the above-mentioned studies with regard to the non-dissipative area affected by different control loops.

The second aspect focuses on the non-dissipative region caused by control loops, which is usually near or below the inner-loop bandwidth [19]–[22]. To suppress the dc-bus oscillation, a high-pass filter based on the dc-voltage feedforward is designed to enhance the dissipativity of the

Manuscript received January 3, 2023; revised March 14, 2023; accepted April 10, 2023. Date of publication December 30, 2023; date of current version May 10, 2023. This work was supported in part by the Fundamental Research Funds for the Central Universities under Grant JZ2023HGTA0183, in part by Science and Technology Project of State Grid Corporation of China under Grant 5108-202218280A-2-321-XG, in part by the Villum Investigator Program funded by the Villum Foundation. *(Corresponding author: Shan He.)*

Z. Yang, W. Wu, H. Li, and L. Ding are with School of Electrical Engineering and Automation, Hefei University of Technology, Hefei 230009, China (e-mail: zhiqing.yang@hfut.edu.cn; wei.wu@mail.hfut.edu.cn; helong.li@hfut.edu.cn; ljding@hfut.edu.cn).

S. He and F. Blaabjerg are with Department of Energy, Aalborg University, Aalborg 9220, Denmark (e-mail: shh@tf.uni-kiel.de; fbl@energy.aau.dk).

Digital Object Identifier 10.24295/CPSSTPEA.2023.00026

dc-link impedance [19]. To mitigate the non-dissipative area caused by the PLL, the *q*-axis impedance is reshaped through a proportional voltage feedforward [20]. A virtual inductor strategy is used to enhance system damping based on the current feedback [21]. In addition, a small bandwidth of the voltage feedforward filter (VFF) is preferred for normal operations, to reduce the non-dissipative region induced by the outer control loops, while the VFF bandwidth can be increased in transients to avoid overcurrent tripping [22]. However, the above-mentioned studies mainly focus on the non-dissipative region induced by a single control loop, and the impact of the control time delay is ignored. According to [11], [12], non-dissipative regions in a system can be affected by multiple control loops simultaneously. The design for a certain frequency range may also influence the property in other frequencies [15], [19], [20].

To cope with non-dissipative regions induced by either the time delay or control loops, this work proposes a unified virtual admittance control (UVAC) scheme for grid-following inverters. Wideband dissipativity can be enhanced by designing different virtual elements following a model-based approach.

The rest of this work is organized as follows. Fundamentals of stability analysis based on admittance models are elaborated in Section II. Based on that, dissipativity properties are investigated to reveal the potential risk of resonances. To enhance system dissipation, a UVAC is proposed in Section III. The dissipation in different frequencies can be flexibly enhanced by designing corresponding virtual elements, following a model-based approach. To realize wideband dissipativity enhancement, a design guideline is proposed in Section IV, based on which the UVAC parameters are tuned for a high-power system. In Section V, validations are presented with detailed simulations and experiments for a down-scaled prototype. Conclusions are given in Section VI.

II. Stability Investigation

A. System Modeling

The schematic of a three-phase grid-following inverter system is shown in Fig. 1, considering the filter components and basic control block diagrams. An LCL filter is designed to suppress switching harmonics, where L_2 can be implemented with the leakage inductance of a transformer. The *dq*-domain alternating-current control (ACC) is considered as the inner loop for current regulation. The PLL measures the grid-side capacitor voltages for grid synchronization. The dc-link voltage is regulated by the DVC, which is often required in renewable energy systems to optimize the power generation. Due to the computation delay and the zero-order hold effect, the pulse-width modulation (PWM) induces a time delay of one and a half sampling period $1.5T_{sp}$. Key parameters of the investigated system are given in Table I, referring to a 2 MVA grid-following inverter system in photovoltaic application [23].

To investigate system stability and reveal the potential resonances, the admittance models developed in the previous

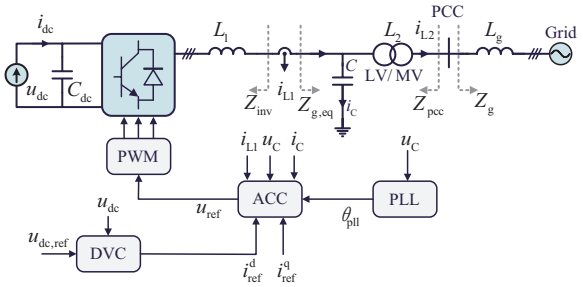

Fig. 1. System diagram of a three-phase grid-following converter system.

TABLE I
System Specifications of a 2 MVA System

Parameter	Value	Parameter	Value
$V_{g,ll}^{rms}$	550 V	S_n	2 MVA
f_{sw}	3 kHz	f_{sp}	6 kHz
L_1 / λ_i	120 μH/18%	C / λ_q	0.4 mF / 2%
C_{dc}	15 mF	L_2	40 μH
f_{ACC}	300 Hz	K_p^{ACC}	0.23
f_{PLL}	30 Hz	K_p^{PLL}	0.36
f_{DVC}	20 Hz	K_p^{DVC}	3.6

work [24] are adopted, to characterize the inverter output port feature through two-dimensional transfer matrices (1). Based on that, the equivalent impedance of an inverter system at the point of common coupling (PCC) can be further obtained by including the filter parameters (2).

$$\begin{bmatrix} \hat{i}_{L1}^{d} \\ \hat{i}_{L1}^{q} \end{bmatrix} = \underbrace{\begin{bmatrix} Y_{inv}^{dd} & Y_{inv}^{dq} \\ Y_{inv}^{qd} & Y_{inv}^{qq} \end{bmatrix}}_{\mathbf{Y}_{inv}} \begin{bmatrix} \hat{v}_{C}^{d} \\ \hat{v}_{C}^{q} \end{bmatrix} \tag{1}$$

$$\mathbf{Z}_{pcc} = \mathbf{Z}_{L2} + 1/\left(\mathbf{Y}_{inv} + \mathbf{Y}_{C}\right) \tag{2}$$

B. Stability Analysis

With the developed admittance models, different methods are available to investigate system stability, which are summarized in Table II.

The Bode criterion evaluates system stability according to the frequency response of two impedances/admittances at an interaction point. Take the PCC as an example, the stability can be evaluated with the inverter impedance seen from the PCC Z_{pcc} and the grid impedance Z_g. Usually, the off-diagonal impedances are negligible comparing to the diagonal ones, so that the stability can be evaluated with diagonal Bode plots. The intersection of two magnitude curves indicates the risk of resonances, and the phase difference of curves shows the stability margin [4], [5]. Bode plots provides an intuitive overview in the frequency-domain, which facilitates analyzing the impedance shaping effect influenced by various factors.

The generalized Nyquist criterion investigates stability with the eigenvalues acquired from the return ratio matrix

TABLE II
DIFFERENT STABILITY ANALYSIS METHODS

Method	Analysis on	Features (+: Pros, -: Cons)	Application
Bode plot [4], [5]	Impedances $\mathbf{Z}_{pcc}$ & $\mathbf{Z}_g$	+: Freq.-domain info, resonance identification -: Inaccurate boundary	Impedance shaping
Nyquist plot [4], [6]	Eigenvalues λ	+: Accurate boundary -: Unintuitive freq.-domain info	Stability boundary
Forbidden-region [7], [8]	Return ratio matrix $\mathbf{L}$	+: Without eigenvalue calculation -: Conservative	Stability margin design
Net-damping [9], [10]	Dissipativity $\mathrm{Re}\{Y(j\omega)\}$	+: Freq.-domain damping, resonance identification -: Not suitable for stability boundary evaluation	Dissipativity design

$\mathbf{L}$ (3) by solving the determinant in (4). A system is stable if none of Nyquist curves of eigenvalues encircle the point $(-1, j0)$ [4], [6]. The Nyquist criterion predicts more accurate stability boundary comparing to the Bode plots, as the impact of off-diagonal elements are also included when calculation eigenvalues [25]. However, the frequency information is hidden in the complex plane, which is inconvenient to directly view the potential resonances. The frequency information is available if the polar plots of Nyquist curves are transferred to the frequency responses [6].

$$\mathbf{L} = \mathbf{Z}_g \cdot \mathbf{Z}_{pcc}^{-1} = \begin{bmatrix} L^{dd} & L^{dq} \\ L^{qd} & L^{qq} \end{bmatrix} \tag{3}$$

$$\lambda_{1,2} = \det[\mathbf{L} - \lambda \mathbf{I}] = 0 \tag{4}$$

Furthermore, the forbidden-region criterion evaluates system stability from geometric perspective. According to Gerschgorin Disc Theorem, eigenvalues of a matrix are distributed in a circle around diagonal elements, with a radius of the sum of off-diagonal elements in the same row (5) [7]. To make sure that all the eigenvalues do not encircle $(-1, j0)$, a forbidden region should be defined, e.g., the left side of $(-1, j0)$. Based on that, the constraint conditions of stability could be derived according to the geometric relations (6). The forbidden-region criterion is usually more conservative than Nyquist criterion, depending on the definition of the forbidden region. Advanced forbidden-region method also facilitates the design of stability margins [8].

$$\left|\lambda_1 - L^{dd}\right| < \left|L^{dq}\right| \quad \text{and} \quad \left|\lambda_2 - L^{qq}\right| < \left|L^{qd}\right| \tag{5}$$

$$\mathrm{Re}\left\{L^{dd}\right\} - \left|L^{dq}\right| > -1 \quad \text{and} \quad \mathrm{Re}\left\{L^{qq}\right\} - \left|L^{qd}\right| > -1 \tag{6}$$

In addition, the net-damping criterion analyzes system stability from the perspective of dissipation, based on the passivity theory. The damping or the dissipativity of a system $G(s)$ can be characterized by its real part value $\mathrm{Re}\{G(j\omega)\}$ in the frequency domain. An interconnected system may result in resonances, if the net damping is negative at corresponding frequencies [26]. For grid-following converter systems, the stability boundary cannot be directly predicted by the dissipativity of the converter admittance. However, the stability is sufficiently guaranteed, if the total damping of the converter and the grid is greater than zero (7) [9], [10]. Hence, it is benefit for system stability with higher damping in wide frequencies.

$$\mathrm{Re}\left\{Y_{inv}(j\omega)\right\} + \mathrm{Re}\left\{Y_{g,eq}(j\omega)\right\} \geqslant 0 \tag{7}$$

Among various methods, the net-damping criterion provides an intuitive approach to analyze the weak point of a system in the frequency domain, without calculating the return ratio matrix or the eigenvalues. Since the grid and filter impedance are assumed to be passive in many applications, a more conservative constraint can be derived to guarantee system stability by observing only the dissipativity of the inverter-admittance $\mathrm{Re}\{Y_{inv}(j\omega)\}$. Recent studies indicate that the dissipativity can be designed to enhance system stability [13]–[22]. To identify the risk of resonances or instability, non-dissipative region shall be first investigated.

C. Dissipativity Investigation

Ideally, a stable system requires positive dissipation over the whole frequency range, i.e., $\mathrm{Re}\{Y_{inv}(j\omega)\} \geqslant 0, \ \forall\omega$. However, this is impossible due to the implemented control loops [4], [6], [11] and the time delay [13]–[18]. Resonances can occur in the frequency range, where the system behaves non-dissipative. To identify the non-dissipative areas of a grid-following inverter including asymmetric control loops, the dissipativity of the two-dimensional inverter admittance matrix Y_{inv} is investigated. It is observed that the off-diagonal elements can be neglected comparing to the diagonal ones [4]. Thus, only the diagonal dissipativity properties are presented.

1) Direct-Voltage Control: Different DVC bandwidths f_{DVC} affect only the *d*-axis dissipation, as the DVC outputs the *d*-axis current reference for the inner loop. A non-dissipative region is observed slightly above the DVC bandwidth, as depicted in Fig. 2. Usually, it is preferred to design the outer loop bandwidth at around one decade below the inner current loop [11]. However, a too small bandwidth is not preferred either, since a decreased DVC bandwidth extends the non-dissipative region and reduces dissipation.

2) Phase-Locked Loop: On contrary to the DVC, different PLL bandwidths f_{PLL} shape only the *q*-axis dissipativity and induce a non-dissipative region within the bandwidth, as presented in Fig. 3. This non-dissipative area is inevitable, as

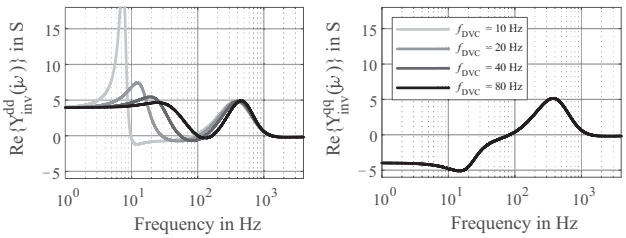

Fig. 2. Frequency-domain dissipation by the DVC.

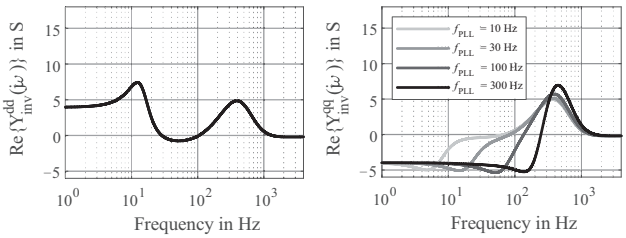

Fig. 3. Frequency-domain dissipation affected by the PLL.

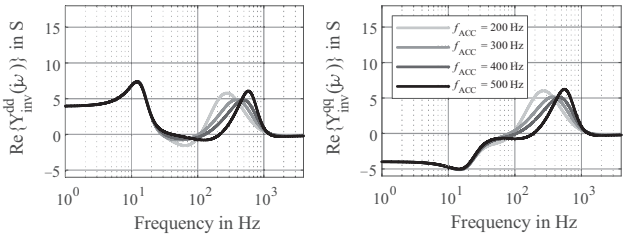

Fig. 4. Frequency-domain dissipation affected by the ACC.

a negative incremental resistance exists in the *q*-axis when the PLL regulates v_C^q for synchronization [4]. Hence, the PLL bandwidth is usually designed as small as possible.

3) Alternating-Current Loop: As illustrated in Fig. 4, the ACC influences both diagonal dissipativity due to its symmetric implementation in the *dq* frame. It is found that the rule of thumb design, i.e., $f_{ACC} \leqslant f_{sw}/10$, presents the optimal dissipation property. Either an increased or decreased bandwidth would enlarge the non-dissipative region.

4) Voltage Feedforward Filter: A voltage feedforward term is preferred to avoid overcurrent tripping during grid disturbances [27]. The VFF is implemented with a diagonal feedforward transfer matrix G_{VFF}. The diagonal elements are in form of a low-pass filter (LPF) $2\pi f_{VFF}/s+2\pi f_{VFF}$, where the bandwidth f_{VFF} can be designed to enhance dissipativity [22]. However, it can induce a non-dissipative area below the inner-loop bandwidth, as depicted in Fig. 5. An increased bandwidth of the VFF extends the non-dissipative region towards higher frequencies, while the high-frequency dissipativity beyond the inner-loop bandwidth is slightly improved. There is no strict rule to select the VFF bandwidth. A coarse design is suggested in [22] to consider a small bandwidth $f_{VFF} \leqslant f_{ACC}/10$ in normal operations to enhance dissipativity, while to increase the bandwidth to $f_{VFF} \geqslant f_{ACC}$ in fault conditions to improve dynamic performance.

5) Time Delay: Due to the computational delay and the

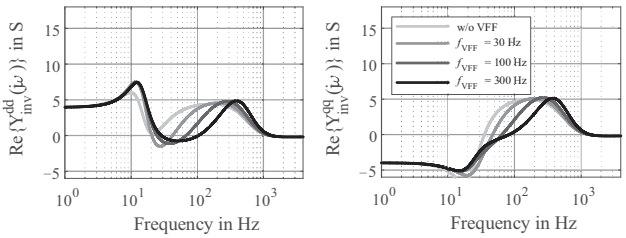

Fig. 5. Frequency-domain dissipation by the VFF.

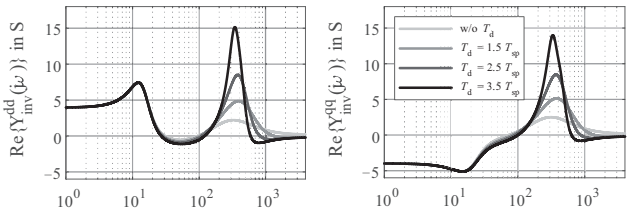

Fig. 6. Frequency-domain dissipation affected by the time delay.

latching effect in modulation, a minimum control time delay of one and a half sampling period $T_d = 1.5T_{sp}$ is usually inevitable [13]–[18]. The time delay in modular multilevel converters is even longer due to the control complexity [28]. As depicted in Fig. 6, the dissipativity near the ACC bandwidth is enhanced with an increased time delay. However, a large time delay induces more negative damping in the high-frequency region and extends the non-dissipative area towards lower frequencies.

In summary, wideband non-dissipative regions are inevitable. The non-dissipative regions below the inner-loop bandwidth are different in the *dq* domain due to asymmetric control implementations. While the non-dissipative regions beyond the inner-loop bandwidth are almost identical, as the time delay has a symmetric impact in the *dq* domain. The non-dissipative regions can lead to wideband resonances if excitations occur.

III. Unified Virtual Admittance Control

To eliminate resonances and improve system stability, a UVAC method is proposed to improve system dissipation over a wide frequency range. The control structure and the model-based parameter tuning approach are introduced in this section.

A. Control Structure

As dissipativity is determined by the characteristics of the converter output admittance, a UVAC utilizing a feedforward structure is proposed to reshape the converter admittances, in order to enhance dissipation. As depicted in Fig. 7, the UVAC consist of a diagonal matrix $\mathbf{G}_{UVAC}$ (8), where the control function is considered in a PID form (9). As the control function links the capacitor voltage to the current referent, the PID-structured control function emulates actually multiple virtual elements in parallel at the grid side. The proportional gain emulates a virtual resistor R_v, the integral gain represents a virtual inductor L_v, and the derivative gain indicates a virtual capacitor C_v. Different virtual element can decouple

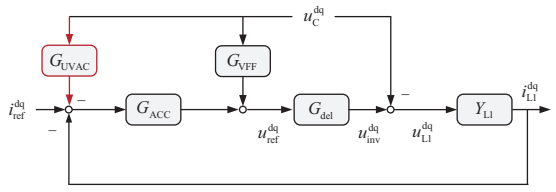

Fig. 7. Control implementation of the unified virtual admittance control.

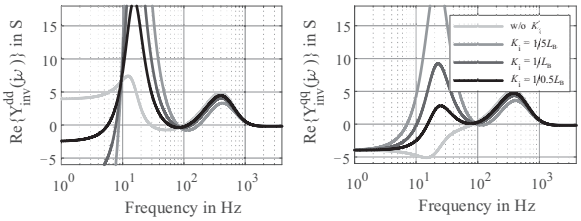

Fig. 8. Dissipativity enhancement in the low-frequency region.

the dissipativity design in the low-, mid- and high-frequency regions, respectively. Based on that, the control parameters can be tuned following a model-based approach.

$$\mathbf{G}_{\mathrm{UVAC}} = \begin{bmatrix} G_{\mathrm{C}}^{\mathrm{dd}} & 0 \\ 0 & G_{\mathrm{C}}^{\mathrm{qq}} \end{bmatrix} \tag{8}$$

$$G_{\mathrm{C}} = K_{\mathrm{p}} + \frac{K_{\mathrm{i}}}{s} + sK_{\mathrm{d}} \tag{9}$$

$$G_{\mathrm{C}}^{\mathrm{ele}} = \frac{1}{R_{\mathrm{v}}} + \frac{1}{sL_{\mathrm{v}}} + sC_{\mathrm{v}} \tag{10}$$

Depending on the system rating, there is no clear boundaries between different frequency ranges. For clarity in this work, the range below the outer loop bandwidth is considered as the low-frequency region, the range between the outer-loop and inner-loop bandwidth is considered as the mid-frequency region, while the range beyond the inner-loop bandwidth is considered as the high-frequency region.

B. Low-Frequency Dissipativity Enhancement

According to Figs. 2 and 3, the low-frequency dissipativity is mainly influenced by the output-loop controls. To improve the dissipativity in the low-frequency region, an integral gain K_{i} is considered. Since K_{i} behaves as a virtual inductor L_{v}, a model-based parameter tuning method is proposed to design L_{v} by referring to the system base inductor value L_{B} (11). As observed in Fig. 8, an increased value of K_{i}, i.e., a decreased value of L_{v}, can significantly enhance the q-axis low-frequency dissipativity without affecting the high frequency region. As for the d-axis design, most of the enhanced regions are already passive, and an increased K_{i} reduces the dissipation below the DVC bandwidth. Hence, K_{i} is preferred only for the q-axis compensation. Although a lower value of L_{v} can further increase damping, the mid-frequency dissipation would decrease either, which should be avoided. As the starting point

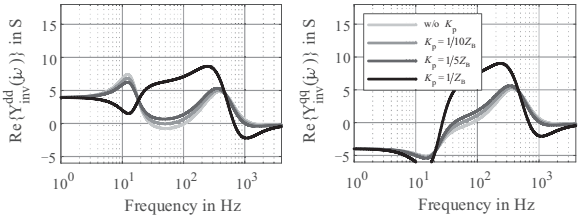

Fig. 9. Dissipativity enhancement in the mid-frequency region.

of the design, $L_{\mathrm{v}} = L_{\mathrm{B}}$ can be considered for the q-axis.

$$K_{\mathrm{i}} = \frac{1}{L_{\mathrm{v}}} = \frac{1}{xL_{\mathrm{B}}} = \frac{\omega_{\mathrm{g}} S_{\mathrm{B}}}{xV_{\mathrm{B}}^2} = \frac{\omega_{\mathrm{g}} S_{\mathrm{n}}}{x\left(V_{\mathrm{g,11}}^{\mathrm{rms}}\right)^2} \tag{11}$$

C. Mid-Frequency Dissipativity Enhancement

According to Figs. 4 and 5, the mid-frequency dissipation is mainly influenced by the ACC and VFF. To improve the dissipation in the mid-frequency area, a proportional damping gain K_{p} is considered. Similar to the design of K_{i}, K_{p} is determined by referring to the system base impedance value Z_{B} (12). According to Fig. 9, an increased value of K_{p}, i.e., a decreased value of R_{v}, can improve the mid-frequency dissipativity. However, both low- and high-frequency dissipation would deteriorate, if the value of R_{v} is too small. As the starting point of the design, $R_{\mathrm{v}} = 5Z_{\mathrm{B}}$ can be considered.

$$K_{\mathrm{p}} = \frac{1}{R_{\mathrm{v}}} = \frac{1}{yZ_{\mathrm{B}}} = \frac{S_{\mathrm{B}}}{yV_{\mathrm{B}}^2} = \frac{S_{\mathrm{n}}}{y\left(V_{\mathrm{g,11}}^{\mathrm{rms}}\right)^2} \tag{12}$$

D. High-Frequency Dissipativity Enhancement

1) Model-Based Parameter Tuning: Summarizing the low and mid-frequency dissipativity enhancement based on the virtual element design, a higher damping is realized by a smaller value of L_{v} or R_{v}, which tends to create a virtual short circuit' in the parallel filter branch, and thus, equivalently reduces the effect of the grid-side capacitor C. Following the same strategy, a model-based design method is proposed to improve the high-frequency dissipativity. Since the derivative damping gain K_{d} represents an equivalent virtual capacitor C_{v}, it can be directly selected as a negative value referring to the grid-side capacitor in the LCL filter to compensate the corresponding counterpart (13). As depicted in Fig. 10, a higher absolute value of K_{d}, i.e., a higher absolute value of C_{v}, can improve the high-frequency dissipation without much affection of both low- and mid-frequency dissipativity. As the starting point of the design, $C_{\mathrm{v}} = -C$ can be considered for systems with a normal time delay $T_{\mathrm{d}} = 1.5T_{\mathrm{sp}}$.

$$K_{\mathrm{d}} = C_{\mathrm{v}} = -zC \tag{13}$$

2) Comparison to Conventional Design: To further explain the compensation logic, the proposed high-frequency

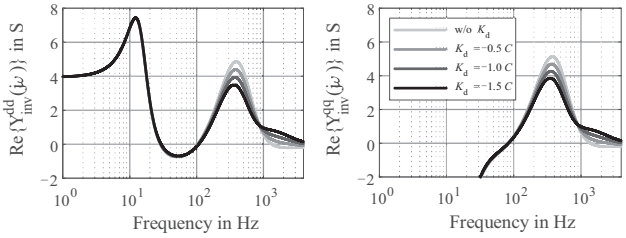

Fig. 10. Dissipativity enhancement in the high-frequency region.

dissipativity design is compared to the conventional method in [13], where a derivative damping gain of the measured ac voltages is fed forward to u_{ref}. The compensation gain K_{ad} is determined according to the total time delay (14). If the design of the ACC follows the model-based approach [29], i.e. $K_{\text{p}}^{\text{ACC}} = \omega_{\text{ACC}} L_1 = 2\pi f_{\text{ACC}} L_1$, the damping gain can also be fed forward to i_{ref} with an equivalent gain $K_{\text{ad}}^{\text{eq}}$, which is the same structure in this work. The integral gain of the ACC is negligible when analyzing the high-frequency feature. Assuming that the time delay $T_{\text{d}} = mT_{\text{sp}} = m/f_{\text{sp}}$, and the sampling frequency $f_{\text{sp}} = nf_{\text{sw}}$, $K_{\text{ad}}^{\text{eq}}$ can be characterized in relation to the converter-side inductor L_1 and the switching frequency f_{sw} (15). Note that $m = 1.5$ if no additional delay is considered, $n = 1$ for the single-update PWM, $n = 2$ for the double-update PWM.

$$K_{\text{ad}} = \frac{4\omega_{\text{ACC}} T_{\text{d}}^2}{\pi^2} \tag{14}$$

$$K_{\text{ad}}^{\text{eq}} = \frac{K_{\text{ad}}}{\omega_{\text{ACC}} L_1} = \frac{4T_{\text{d}}^2}{\pi^2 L_1} = \frac{4m^2}{\pi^2 L_1 f_{\text{sp}}^2} = \frac{m^2}{n^2} \cdot \frac{4}{\pi^2 L_1 f_{\text{sw}}^2} \tag{15}$$

The proposed model-based approach (13) determines K_{d} according to the value of the filter capacitor, which is also determined by L_1 and f_{sw}, according to the standard filter design procedure. Usually, L_1 is determined by the desired current ripple Δi_{L1} according to the factor λ_{i} (16), while C is designed according to the power factor requirement depending on the factor λ_{q} (17) [30]. The ac and dc voltages are linked via the modulation index M (18). Usually, an inverter system is preferred to operate with a high modulation index, i.e., $M \rightarrow 1$. Combining (16)–(18), the value of C can be determined by L_1, f_{sw}, λ_{i}, and λ_{q} (19). The LC filters of the 2 MVA system in this work are designed with $\lambda_{\text{i}} = 18\%$ and $\lambda_{\text{q}} = 2\%$ following the recommendation in [30], [31].

$$L_1 = \frac{\sin\left(\frac{2\pi}{3}\right) V_{\text{dc}} M}{6\Delta i_{\text{L1}} f_{\text{sw}}} = \frac{1}{\lambda_{\text{i}}} \cdot \frac{\sqrt{3} V_{\text{dc}} M}{12 I_{\text{n}} f_{\text{sw}}} \tag{16}$$

$$C = \frac{\lambda_{\text{q}} S_{\text{n}}}{3\omega_{\text{g}} V_{\text{g}}^2} = \lambda_{\text{q}} \cdot \frac{I_{\text{n}}}{\omega_{\text{g}} V_{\text{g}}} \tag{17}$$

$$M \cdot \frac{V_{\text{dc}}}{2} = \sqrt{2} V_{\text{g}} \tag{18}$$

$$C = \frac{\lambda_{\text{q}}}{\lambda_{\text{i}}} \cdot \frac{1}{\sqrt{6}\omega_{\text{g}} L_1 f_{\text{sw}}} \tag{19}$$

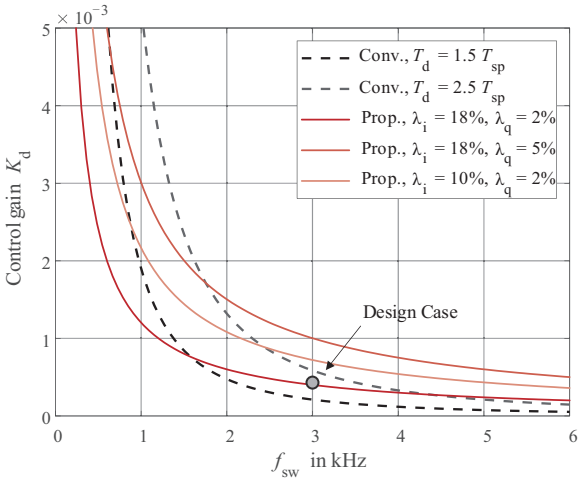

Fig. 11. Damping gain comparison of the 2 MVA system.

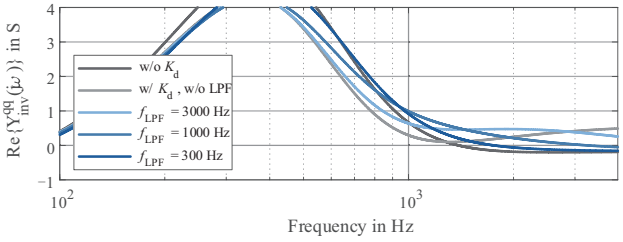

Fig. 12. Dissipativity affected by the derivative gain with the LPF.

According to the designed filters specified in Table I, the proposed design is compared to the conventional method for different time delays, as depicted in Fig. 11. The higher the value of f_{sw}, the more dissipation can be provided with the proposed method. The proposed design is able to provide higher damping compared to the conventional method for the operation with $f_{\text{sw}} \geqslant 2$ kHz, considering a normal time delay $1.5T_{\text{sp}}$. To achieve better filtering of harmonics, the filters can be designed with a higher value of λ_{q} or a lower value of λ_{i}, which represents a higher value of C or L_1, respectively. In both cases, the damping performance of the proposed method increases further.

3) Practical Implementation: A pure derivative gain induces actually a narrow dissipation dip in the high-frequency area as depicted in Fig. 12. An additional bi-quad filter is suggested for optimization, which requires further efforts for parameter tuning [13], [16]. Considering the practical implementation in this work, the derivative term is multiplied with a low-pass filter (LPF) with the bandwidth $\omega_{\text{LPF}} = 2\pi f_{\text{LPF}}$ (20). The LPF can not only alleviate the dissipation dip, but also prevent the noise amplification. A decreased LPF bandwidth reduces the compensation effect, which can even induce a non-dissipative area in the high-frequency region. Thus, it is recommended to consider $f_{\text{ACC}} < f_{\text{LPF}} < f_{\text{sw}}/2$.

$$s \rightarrow \frac{\omega_{\text{LPF}}}{s + \omega_{\text{LPF}}} \cdot s \tag{20}$$

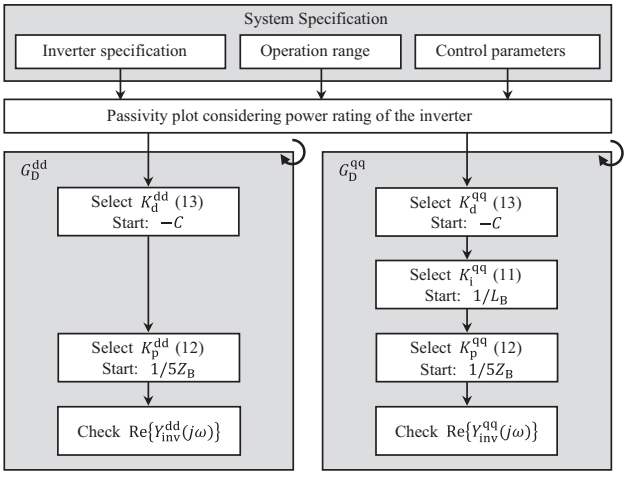

Fig. 13. Wideband dissipativity design guideline.

As a summary, the proposed UVAC can effectively improve the wideband dissipativity in the *dq* domain. Based on the system rating and filter parameters, the PID-based control gains, which serve as virtual electrical elements, can be designed following a model-based approach. Since overlapping influences are observed between individual damping gains, a proper design procedure shall be considered as well.

IV. Wideband Dissipativity Design

To achieve satisfied wideband dissipativity design with the UVAC, a design procedure is developed in this section. Following that, wideband dissipativity property of a 2 MVA system is designed. The stability improvement with the UVAC is investigated in different scenarios.

A. Design Guideline

Observing Figs. 8−10, the high-frequency dissipativity enhancement with K_d has quite limited influence on other frequency ranges, while K_p can induce significant dissipation dip in both low and high-frequency areas, which affects the compensation of other damping gains. To realize the wideband dissipativity improvement with the UVAC, a design guideline is proposed as illustrated in Fig. 13, considering a certain design sequence and initial values. First, the dissipativity in the *dq* domain are observed for the analyzed system, in order to overview in which frequency ranges non passive regions occur. Following the model-based approach (11)−(13), the control gains are designed step by step for individual frequency ranges. It is suggested to design K_d firstly, while consider K_p lastly. Based on suggested starting value, iterations can be considered to further adjust the parameters for optimization.

B. Design Case

1) Parameter Tuning: A design example is elaborated for the studied 2 MVA system step by step, as depicted in Fig. 14. K_d and K_p are considered to enhance the *d*-axis dissipativity in the mid- and high-frequency areas. The low-frequency

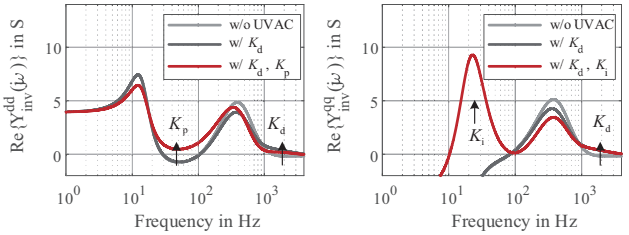

Fig. 14. Wideband dissipativity enhancement for the 2 MVA system.

TABLE III
UVAC Parameters for a 2 MVA System

Parameter	Value	Parameter	Value
Z_B	150 mΩ	L_B	480 μH
K_d^d	$-C$	K_d^q	$-C$
K_i^d	0	K_i^q	$1/L_B$
K_p^d	$1/6Z_B$	K_p^q	0

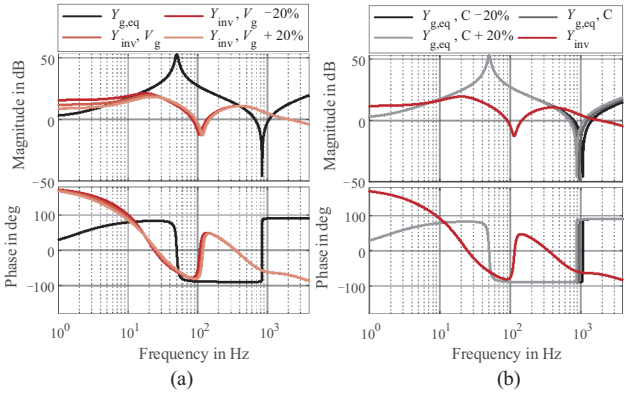

Fig. 15. Robustness analyses of the designed dissipativity. (a) Variation of V_g. (b) Variation of C.

area is naturally passive, since the PLL only affects the *q*-axis admittance. K_d and K_i are considered to enhance the *q*-axis dissipativity in the low- and high-frequency ranges. The *q*-axis mid-frequency region is originally passive, because the DVC influences only the *d*-axis admittance. The designed parameters are provided in Table III.

2) Robustness Analysis: Since the virtual elements are designed according to the grid-side voltage and the capacitor value, robustness analyses are conducted considering ±20% parameter variations. The *q*-axis admittances shown in Fig. 15 are considered as an example, the variation of V_g slightly influences Y_{inv}^{qq} in the low-frequency area, while the variation of C has an impact on the grid-side equivalent admittance $Y_{g,eq}^{qq}$ in the high-frequency region. However, the designed dissipativity is not influenced, since the angle of Y_{inv}^{qq} still remains within ±90° over a wide frequency range.

C. Design Validation

To prove the validity of the proposed control scheme, two different scenarios are considered, as depicted in Fig. 16. Case

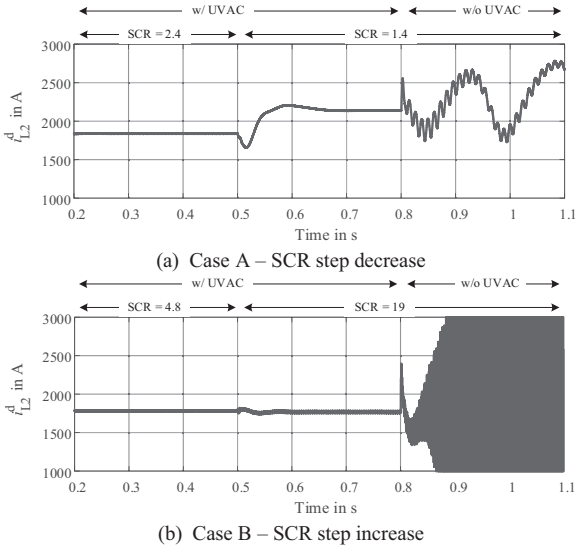

Fig. 16. Validation of the proposed design method.

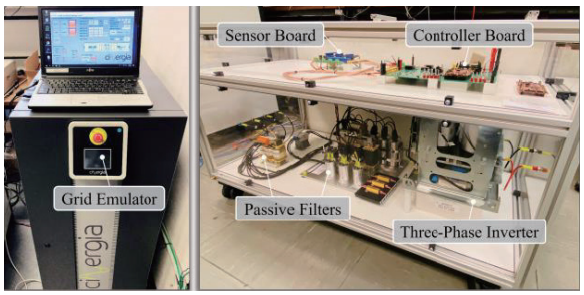

Fig. 17. Experimental setup.

A investigates an operation under weak grid with a low short-circuit ratio (SCR), considering a step change of the SCR from 2.4 (L_g = 200 μH) to 1.4 (L_g = 350 μH). The system stability is guaranteed with the UVAC, while resonances occur once the UVAC is deactivated. Low-frequency resonances occur, which correspond to the low-frequency non-dissipative region of the original system, according to Fig. 14.

Case B considers a normal-grid operation, considering a step change of the SCR from 4.8 (L_g = 100 μH) to 19 (L_g = 150 μH). A decreased L_g shifts the potential resonances towards higher frequencies. The system remains stabilized if the UVAC is implemented, while the stability is not guaranteed if the UVAC is deactivated. High-frequency resonances occur, which are caused by the high-frequency non-dissipative region of the original system as shown in Fig. 14.

The investigated scenarios validate effectiveness of the proposed UVAC. Resonances can be eliminated if the dissipativity is enhanced at corresponding frequencies.

V. Verification With Down-Scaled Prototype

The effectiveness of the UVAC is further validated with a down-scaled prototype. As depicted in Fig. 17, the test setup consists of an inverter, passive filters, control and sensor boards, and a grid emulator. Key specifications of the down-scaled system are provided in Table IV. Following the proposed design procedure, virtual elements are designed for the down-scaled system as well.

TABLE IV
System Specifications of a 1 kVA System

Parameter	Value	Parameter	Value
$V_{g,ll}^{rms}$	110 V	S_n	1 kVA
f_{sw}	10 kHz	f_{sp}	10 kHz
L_i / λ_i	2.5 mH / 20%	C / λ_q	10 μF / 4%
f_{ACC}	1000 Hz	K_p^{ACC}	16
f_{PLL}	30 Hz	K_p^{PLL}	1.8
Z_B	12 Ω	L_B	38 mH
K_d^{dd}	$-C$	K_d^{qq}	$-C$
K_i^{dd}	0	K_i^{qq}	$1/L_B$
K_p^{dd}	$1/4Z_B$	K_p^{qq}	$1/4Z_B$

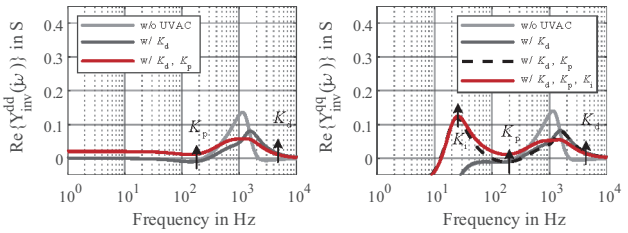

Fig. 18. Wideband dissipativity enhancement for the 1 kVA system.

The dissipativity of the down-scaled system are presented in Fig. 18. Originally, non-dissipative regions are observed over a wide frequency range in both diagonal admittances. Utilizing the proposed UVAC, wideband dissipation can be enhanced by designing different virtual elements.

To verify the performance improvement after the wideband dissipativity enhancement, four different scenarios are considered. Case 1 and Case 2 aim to verify the benefit to enhance dissipation in the low- and mid-frequency region, while Case 3 and Case 4 aim to validate the necessity of enhancing high-frequency dissipativity.

A. Case 1 – Low SCR

Case 1 validates the enhanced system stability for a weak-grid operation. Since filters are limited in the laboratory, Case 1 is verified with simulations. As observed in Fig. 19(a), resonances occur if the SCR decreases to 2.5 (L_g = 15 mH). The induced resonances are observed at 130 Hz and 230 Hz in the *abc* frame with Fourier analysis, which corresponds to the resonances at 180 Hz in the *dq* frame considering the 50 Hz frequency shift between the *abc* and *dq* frames. By further analyzing the dissipativity property, it is found that the induced resonances fall exactly into the non-dissipative region as depicted in Fig. 19(b), which explains the cause of resonances. After implementing the UVAC, the non-dissipative area at corresponding frequency can be reduced, so that the induced resonances disappear. The system stability can be guaranteed

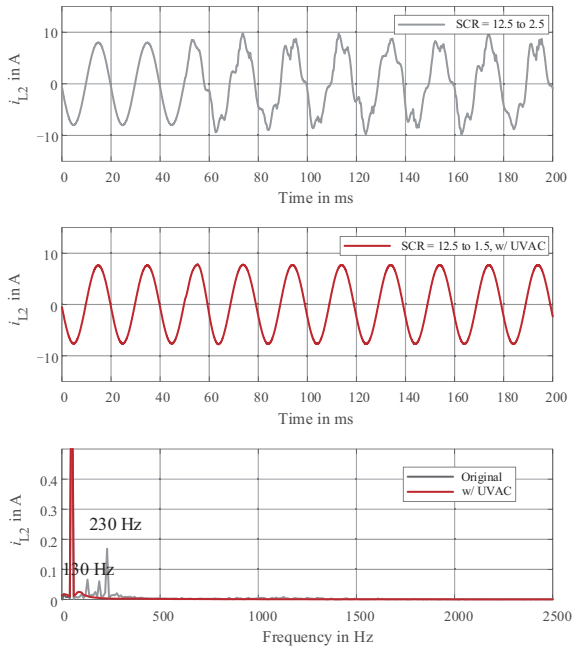

(a) Simulation results

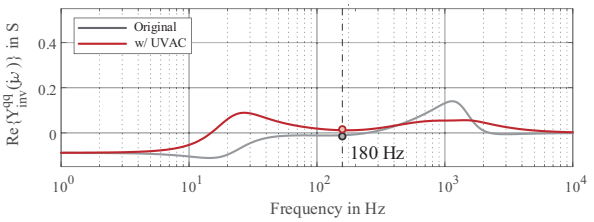

(b) Dissipativity analyses

Fig. 19. Validation of Case 1 (step change of L_g).

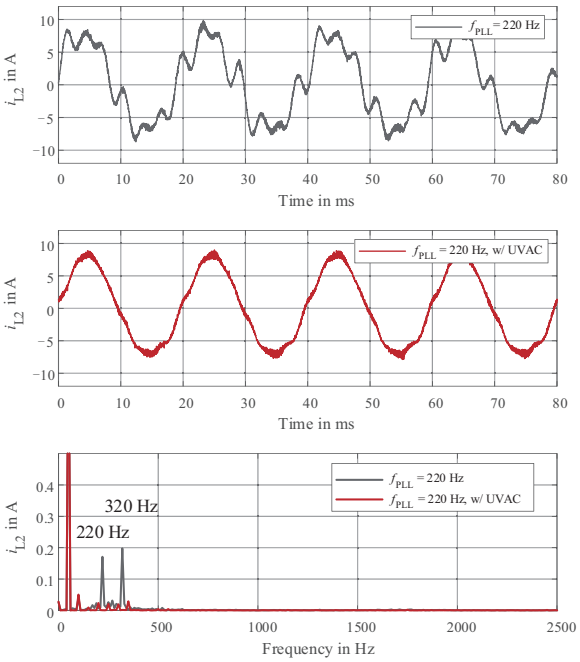

(a) Experiment results

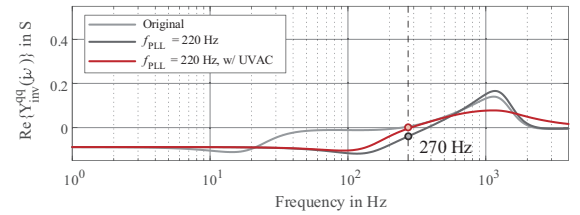

(b) Dissipativity analyses

Fig. 20. Validation of Case 2 (f_{PLL} = 220 Hz).

even for the weak-grid operation until SCR = 1.5 (L_g = 25 mH).

B. Case 2 – High PLL Bandwidth

Case 2 investigates the stability enhancement for a normal operation with a grid impedance of 3 mH (SCR = 12.5). To emulate an unstable scenario, an increased PLL bandwidth f_{PLL} = 220 Hz is implemented, which intentionally increases the non-dissipative area of Y_{inv}^{qq} to the mid-frequency region. As a result, resonances at 220 Hz and 320 Hz are observed in the *abc* frame, as shown in Fig. 20(a), which indicates the resonance at 270 Hz in the *dq* frame. By further analyzing the dissipativity feature, non-dissipative region is also observed at 270 Hz. Positive dissipation can be realized at corresponding frequency after implementing the UVAC, so that the resonance dissipates. Although the low-frequency non-dissipative area cannot be fully compensated with the high PLL bandwidth, resonances disappear, which indicates the necessity of the dissipativity enhancement.

C. Case 3 – Large Time Delay

Case 3 investigates the effectiveness of the UVAC to improve the high-frequency dissipativity. The passive filters of the down-scaled experimental setup are designed with

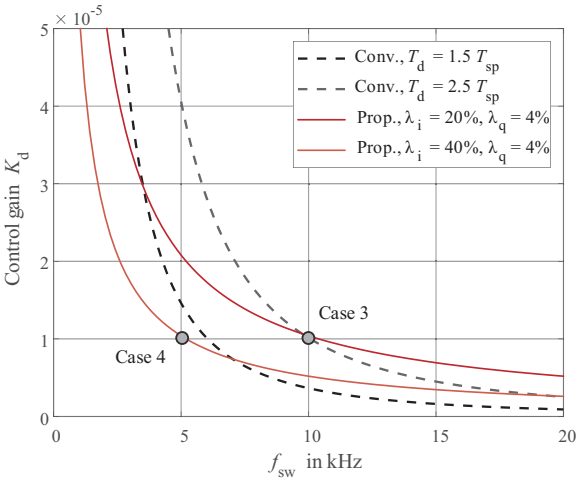

Fig. 21. Damping gain comparison of the 1 kVA system.

λ_i = 20% and λ_q = 4%. Following the proposed model-based approach, K_d is equivalent to a damping gain to compensate $T_d = 2.5T_{sp}$, comparing to the conventional method for the operation with f_{sw} = 10 kHZ, as depicted in Fig. 21. To emulate an unstable case, an additional time delay is implemented, which intentionally deteriorates the high-frequency dissipation.

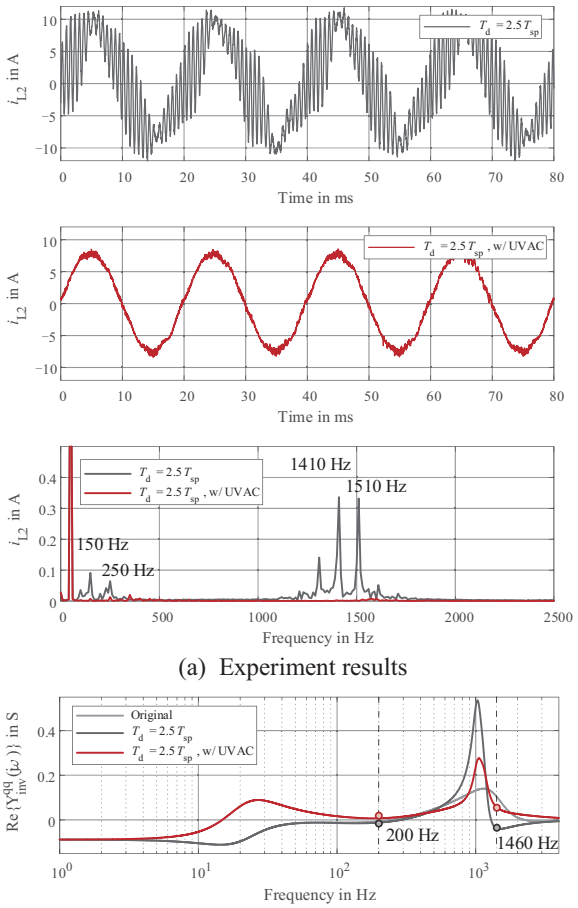

(a) Experiment results

(b) Dissipativity analyses

Fig. 22. Validation of Case 3 ($T_d = 2.5T_{sp}$).

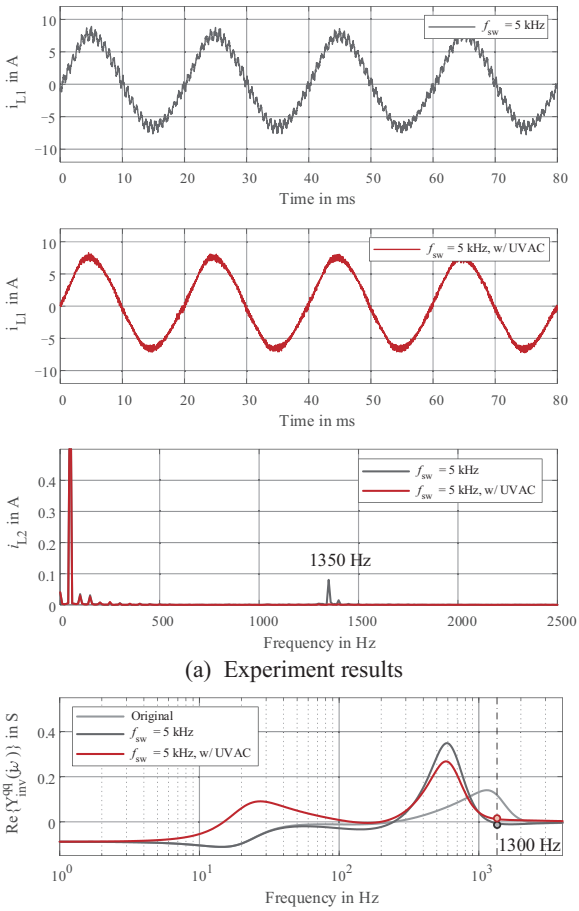

(a) Experiment results

(b) Dissipativity analyses

Fig. 23. Validation of Case 4 ($f_{sw} = 5$ kHz).

As a result, high-frequency resonances at 1410 Hz and 1510 Hz occurs, and low-frequency resonances at 150 Hz and 250 Hz are also observed. By further analyzing the dissipativity feature, it is found that resonant frequencies are located in the non-dissipative region, as presented in Fig. 22(b). After implementing the UVAC, dissipation is enhanced in both low- and high-frequency range. Thus, wideband resonances are eliminated simultaneously.

D. Case 4 – Reduced Switching and Sampling frequency

Case 4 investigates the validity of the high-frequency dissipativity enhancement considering a normal time delay of $1.5T_{sp}$. However, the switching and sampling frequency are intentionally reduced to f_{sw} = 5 kHz, which doubles the control time delay. Note that the ACC bandwidth is also redesigned as f_{ACC} = 500 Hz, following the rule of thumb $f_{ACC} = f_{sw}/10$. As a result, the resonance at 1350 Hz occurs, as depicted in Fig. 23(a). Through the dissipativity analysis, it is found that the resonance falls into the non-dissipative region. After implementing the UVAC, wideband dissipativity enhancement can be realized, so that the resonance disappears. The dissipativity improvement in Case 4 is less obvious than that in Case 3. With a lower switching frequency, the proposed design referring to the capacitor value provides less damping compared to the conventional method due to an increased sampling time. In this case, λ_i becomes doubled with the half switching frequency and the same value of L_1, according to (16). Experimental results prove the validity of the dissipativity enhancement with the proposed control method.

VI. Conclusion

From an energy dissipation point of view, this work evaluates the stability of grid-following inverter systems based on the passivity theory. Utilizing the two-dimensional admittances, the dissipation characteristics of the system is thoroughly investigated over a wide frequency range, which considers the impact of multiple control loops and the time delay, simultaneously. To improve system stability, a UVAC is proposed to enhance wideband dissipativity by designing virtual elements. A design method is proposed to tune the control parameters following a model-based approach, which applies to systems of different power ratings. The effectiveness of the UVAC is validated with simulations and experimental results considering various cases.

References

[1] C. Li, "Unstable operation of photovoltaic inverter from field

experiences," in *IEEE Transactions on Power Delivery*, vol. 33, no. 2, pp. 1013–1015, Apr. 2018.
[2] X. Wang and F. Blaabjerg, "Harmonic stability in power electronic-based power systems: concept, modeling, and analysis," in *IEEE Transactions on Smart Grid*, vol. 10, no. 3, pp. 2858–2870, May 2019.
[3] J. Sun, G. Wang, X. Du, and H. Wang, "A theory for harmonics created by resonance in converter-grid systems," in *IEEE Transactions on Power Electronics*, vol. 34, no. 4, pp. 3025–3029, Apr. 2019.
[4] B. Wen, D. Dong, D. Boroyevich, R. Burgos, P. Mattavelli, and Z. Shen, "Impedance-based analysis of grid-synchronization stability for three-phase paralleled converters," in *IEEE Transactions on Power Electronics*, vol. 31, no. 1, pp. 26–38, Jan. 2016.
[5] M. Amin and M. Molinas, "Understanding the origin of oscillatory phenomena observed between wind farms and HVDC systems," in *IEEE Journal of Emerging and Selected Topics in Power Electronics*, vol. 5, no. 1, pp. 378–392, Mar. 2017.
[6] D. Lu, X. Wang, and F. Blaabjerg, "Impedance-based analysis of DC-link voltage dynamics in voltage-source converters," in *IEEE Transactions on Power Electronics*, vol. 34, no. 4, pp. 3973–3985, Apr. 2019.
[7] Y. Liao, Z. Liu, G. Zhang, and C. Xiang, "Vehicle-grid system modeling and stability analysis with forbidden region-based criterion," in *IEEE Transactions on Power Electronics*, vol. 32, no. 5, pp. 3499–3512, May 2017.
[8] Y. Zhou, H. Hu, J. Yang, and Z. He, "A novel forbidden-region-based stability criterion in modified sequence-domain for AC grid-converter system," in *IEEE Transactions on Power Electronics*, vol. 34, no. 4, pp. 2988–2995, Apr. 2019.
[9] G. Stamatiou and M. Bongiorno, "Stability analysis of two-terminal VSC-HVDC systems using the net-damping criterion," in *IEEE Transactions on Power Delivery*, vol. 31, no. 4, pp. 1748–1756, Aug. 2016.
[10] M. Cheah-Mane, L. Sainz, J. Liang, N. Jenkins, and C. E. Ugalde-Loo, "Criterion for the electrical resonance stability of offshore wind power plants connected through HVDC links," in *IEEE Transactions on Power Systems*, vol. 32, no. 6, pp. 4579–4589, Nov. 2017.
[11] L. Harnefors, M. Bongiorno, and S. Lundberg, "Input-admittance calculation and shaping for controlled voltage-source converters," in *IEEE Transactions on Industrial Electronics*, vol. 54, no. 6, pp. 3323–3334, Dec. 2007.
[12] D. Wang, L. Liang, L. Shi, J. Hu, and Y. Hou, "Analysis of modal resonance between PLL and DC-link voltage control in weak-grid tied VSCs," in *IEEE Transactions on Power Systems*, vol. 34, no. 2, pp. 1127–1138, Mar. 2019.
[13] L. Harnefors, A. G. Yepes, A. Vidal, and J. Doval-Gandoy, "Passivity-based controller design of grid-connected VSCs for prevention of electrical resonance instability," in *IEEE Transactions on Industrial Electronics*, vol. 62, no. 2, pp. 702–710, Feb. 2015.
[14] E. Rodriguez-Diaz, F. D. Freijedo, J. M. Guerrero, J. -A. Marrero-Sosa, and D. Dujic, "Input-admittance passivity compliance for grid-connected converters with an LCL filter," in *IEEE Transactions on Industrial Electronics*, vol. 66, no. 2, pp. 1089–1097, Feb. 2019.
[15] H. Wu and X. Wang, "Virtual-flux-based passivation of current control for grid-connected VSCs," in *IEEE Transactions on Power Electronics*, vol. 35, no. 12, pp. 12673–12677, Dec. 2020.
[16] A. Akhavan, H. R. Mohammadi, J. C. Vasquez, and J. M. Guerrero, "Passivity-based design of plug-and-play current-controlled grid-connected inverters," in *IEEE Transactions on Power Electronics*, vol. 35, no. 2, pp. 2135–2150, Feb. 2020.
[17] Y. Liao, X. Wang, and F. Blaabjerg, "Passivity-based analysis and design of linear voltage controllers for voltage-source converters," in *IEEE Open Journal of the Industrial Electronics Society*, vol. 1, pp. 114–126, 2020.
[18] L. Harnefors, R. Finger, X. Wang, H. Bai, and F. Blaabjerg, "VSC input-admittance modeling and analysis above the nyquist frequency for passivity-based stability assessment," in *IEEE Transactions on Industrial Electronics*, vol. 64, no. 8, pp. 6362–6370, Aug. 2017.
[19] A. Riccobono and E. Santi, "Positive feedforward control of three-phase voltage source inverter for DC input bus stabilization with experimental validation, " in *IEEE Transactions on Industry Applications*, vol. 49, no. 1, pp. 168–177, Jan.-Feb. 2013.
[20] J. Fang, X. Li, H. Li, and Y. Tang, "Stability improvement for three-phase grid-connected converters through impedance reshaping in quadrature-axis," in *IEEE Transactions on Power Electronics*, vol. 33, no. 10, pp. 8365–8375, Oct. 2018.
[21] A. Adib and B. Mirafzal, "Virtual inductance for stable operation of grid-interactive voltage source inverters," in *IEEE Transactions on Industrial Electronics*, vol. 66, no. 8, pp. 6002–6011, Aug. 2019.
[22] L. Harnefors, L. Zhang, and M. Bongiorno, "Frequency-domain passivity-based current controller design," in *IET Power Electronics*, vol. 1, no. 4, pp. 455–465, Dec. 2008.
[23] SMA. Datasheet of sunny centeral. [Online]. Available: https://files.sma.de/downloads/SC4xxxUP-DS-en-30.pdf.
[24] Z. Yang, C. Shah, T. Chen, L. Yu, P. Joebges, and R. W. De Doncker, "Stability investigation of three-phase grid-tied PV inverter systems using impedance models," in *IEEE Journal of Emerging and Selected Topics in Power Electronics*, vol. 10, no. 3, pp. 2672–2684, Jun. 2022.
[25] Z. Yang, W. Gou, X. Luo, C. Shah, N. R. Averous, and R. W. De Doncker, "Stability investigation of three-phase grid-tied PV inverters with impedance-based method," in *2020 22nd European Conference on Power Electronics and Applications (EPE'20 ECCE Europe)*, Lyon, France, 2020, pp. 1–10.
[26] L. Harnefors, "Proof and application of the positive-net-damping stability criterion," in *IEEE Transactions on Power Systems*, vol. 26, no. 1, pp. 481–482, Feb. 2011.
[27] C. H. Van Der Broeck, S. A. Richter, J. V. Bloh, and R. W. De Doncker, "Methodology for analysis and design of discrete time current controllers for three-phase PWM converters," in *CPSS Transactions on Power Electronics and Applications*, vol. 3, no. 3, pp. 254–264, Sept. 2018.
[28] C. Zou, H. Rao, S. Xu, Y. Li, W. Li, J. Chen, X. Zhao, Y. Yang, and B. Lei, "Analysis of resonance between a VSC-HVDC converter and the AC grid," in *IEEE Transactions on Power Electronics*, vol. 33, no. 12, pp. 10157–10168, Dec. 2018.
[29] L. Harnefors and H. -P. Nee, "Model-based current control of AC machines using the internal model control method," in *IEEE Transactions on Industry Applications*, vol. 34, no. 1, pp. 133–141, Jan.-Feb. 1998.
[30] M. Liserre, F. Blaabjerg, and S. Hansen, "Design and control of an LCL-filter-based three-phase active rectifier," in *IEEE Transactions on Industry Applications*, vol. 41, no. 5, pp. 1281–1291, Sept.-Oct. 2005.
[31] X. Ruan, X. Wang, D. Pan, D. Yang, W. Li, and C. Bao, *Control techniques for LCL-type grid-connected inverters*, 2018. Springer, Singapore.

Zhiqing Yang received the B.S. degree from Southwest Jiaotong University, Chengdu, China, in 2013, and the M.S. and Dr.-Ing. degrees from RWTH Aachen University, Aachen, Germany, in 2017 and 2021, respectively, all in electrical engineering.

From April 2016 to September 2016, he was a Research Intern with Advanced Technology R&D Center, Mitsubishi Electric, Amagasaki, Japan. He is currently an Associate Professor with the School of Electrical Engineering and Automation, Hefei University of Technology, and is with the Institute of Energy, Hefei Comprehensive National Science Center. His research interests include power electronics in renewable generations and automobile applications, power converters with wide-bandgap semiconductors.

Dr. Yang serves as the Guest Editor of *CPSS Transactions on Power Electronics and Applications.*

Wei Wu received the B.S. degree in electrical engineering from Dalian Jiaotong University, Dalian, China, in 2018. He is currently pursuing the Ph.D. degree in electrical engineering with Hefei University of Technology, Hefei, China.

His research interests include the field of modeling and control of power converters in renewable generations.

Helong Li received the B.S. and M.S. degrees in electrical engineering from the Harbin Institute of Technology, Harbin, China, in 2010 and 2012, respectively, and the Ph.D. degree in electrical engineering from the Department of Energy Technology, Aalborg University, Aalborg, Denmark, in 2015.

From 2016 to 2019, he was with the Dynex Semiconductor, Ltd., Lincoln, U.K., where he was involved in focusing on power semiconductor packaging. From 2019 to 2021, he was with Cree Europe GmbH, Unterschleissheim, Germany, where he was focusing on silicon carbide (SiC) devices in automotive applications. He is currently a Professor with the School of Electrical and Automation Engineering, Hefei University of Technology, Hefei, China, and is also with the Institute of Energy, Hefei Comprehensive National Science Center, Hefei. His research interests include advanced power semiconductor packaging techniques, and power electronics applications of wide-bandgap power semiconductors.

Dr. Li is the Guest Editor of *IEEE Open Journal of Power Electronics*.

Lijian Ding received the B.S. degree and the M.S. degree in electrical materials and insulation technology from the Harbin Institute of Electrical Engineering, Harbin, China, in 1992 and 1995, respectively, the Ph.D. degree in theory and new technology of electrical engineering from the North China Electric Power University, Beijing, China, in 2000.

He is currently a Professor with the School of Electrical Engineering and Automation, Hefei University of Technology, Hefei, China. He also leads the Institute of Energy, Hefei Comprehensive National Science Center. His research interests include high-voltage technology and fault identification, EMC and reliability of wide-bandgap power semiconductors and power electronic systems.

Shan He received the B.S. degree from Northeast Electric Power University, Jilin, China, in 2015, the M.S. degree from Zhejiang University, Hangzhou, China, in 2018, and the Ph.D. degree from Aalborg University, Aalborg, Denmark, in 2022, all in electrical engineering.

He is currently a Postdoc Fellow with the Department of Energy, Aalborg University. From October to December 2021, he was a visiting researcher with RWTH Aachen University, Aachen, Germany. His current research interests include modeling and control of power converters in renewable generation system, Power-to-X, and battery health management.

Frede Blaabjerg received the Ph.D. degree in electrical engineering from Aalborg University, Aalborg, Denmark, in 1995, and the honoris causa degrees from the Universitatae Politehnica Timisoara, Timisoara, Romania, and TalTech—Tallinn University of Technology, Tallinn, Estonia, in 2017 and 2018, respectively.

He was with ABB-Scandia, Randers, Denmark, from 1987 to 1988. In 1992, he became an Assistant Professor with Aalborg University, an Associate Professor in 1996, and a Full Professor of power electronics and drives in 1998, where he has been a Villum Investigator since 2017. He has authored or coauthored more than 600 journal papers in the fields of power electronics and its applications. He has coauthored four monographs and edited ten books in power electronics and its applications. His current research interests include power electronics and its applications, such as in wind turbines, PV systems, reliability, harmonics, and adjustable speed drives.

Dr. Blaabjerg served as the President of the IEEE Power Electronics Society from 2019 to 2020. He has been the Vice President of the Danish Academy of Technical Sciences. He has received 33 IEEE prize paper awards, the IEEE PELS Distinguished Service Award in 2009, the EPE-PEMC Council Award in 2010, the IEEE William E. Newell Power Electronics Award in 2014, the Villum Kann Rasmussen Research Award in 2014, the Global Energy Prize in 2019, and the 2020 IEEE Edison Medal. He was the Editor-in-Chief of the *IEEE Transactions on Power Electronics* from 2006 to 2012. He was nominated by Thomson Reuters to be among the most 250 cited researchers in engineering in the world for 2014–2020.